ADVANCED FUNCTIONAL MATERIALS
www.afm-journal.de

Multifunctional Dual-Metal-Salt Derived Ternary Eutectic Electrolyte for Highly Reversible Zinc Ion Battery

Jianhui Li, Siqi Qin, Mi Xu, Wei Wang, Jiabin Zou, Yongguang Zhang, Haozhen Dou,* and Zhongwei Chen**

Deep eutectic electrolytes offer opportunities for tailoring solvation structure and interface chemistry in advanced batteries, but developing deep eutectic electrolytes for high-performance zinc ion batteries (ZIBs) remains a challenge. Herein, multifunctional dual-metal-salt derived ternary eutectic electrolytes (DMEEs) are designed via a supporting salt strategy for dendrite-free and long-lifespan ZIBs. DMEEs are constructed by zinc trifluoromethanesulfonate ($Zn(OTF)_2$), supporting salt of lithium bis(trifluoromethanesulfonyl)imide, and neutral ligand of N-methylacetamide. Noticeably, supporting salt with weak lattice energy not only induces the reconstruction of intermolecular interactions to form ion pairs and ion aggregates but also tailors the Zn^{2+} solvation structure and solid electrolyte interface (SEI). The developed DMEEs possess a dual-anion-rich Zn^{2+} solvation shell and induce an inorganic-rich hybrid SEI, which effectively suppresses side reactions and obtains a dendrite-free Zn anode with high reversibility. Remarkably, Zn//Zn cells demonstrate cycling stability for over 3000 h, and Zn//PANI full cells deliver no significant capacity decay after 5000 cycles at a high current density of 5 A g^{-1}. This work opens a new avenue to design advanced deep eutectic electrolytes, and the deep understanding of solvation structure and SEI offers guidelines for developing high-performance batteries.

1. Introduction

Developing renewable energy such as solar and wind power is an important way to alleviate energy pressure and environmental problems,[1–5] which has triggered an ever-increasing demand for designing safe, environmentally friendly, and cost-effective large-scale energy storage technology.[6–9] Among a series of energy storage technologies, lithium-ion batteries (LIBs) are the mainstream due to their high energy density and technical maturity.[10–15] However, the growing cost of electrode materials and the safety issues associated with toxic and flammable organic solvent electrolytes have motivated researchers to develop reliable complementary battery technology.[16–19] Rechargeable zinc ion batteries (ZIBs) have received great attention due to their high safety, low cost, high theoretical capacity, and other remarkable features of easy manufacturing and environmental friendliness.[20–22] However, the practical application of ZIBs faces challenges, the abundant thermodynamically-active H_2O molecules of aqueous electrolytes react with Zn anode, which subsequently leads to the hydrogen evolution reaction (HER), corrosion, and dendrites,[23–26] thus jeopardizing the cycling stability of ZIB and posing safety concerns. Various strategies have been proposed for addressing these issues, such as electrolyte additives,[27–29] zinc anode alloying,[30,31] and constructing artificial protective layers.[32,33] Despite great progress, achieving highly reversible and dendrite-free Zn anode using aqueous electrolytes still remains a challenge, these strategies have not fundamentally prevented the side reactions due to the existence of thermodynamically active H_2O.

Deep eutectic electrolytes (DEEs) are typically obtained by simply mixing Lewis acids and bases in the suitable molar ratios.[34–36] DEEs are featured with excellent thermal stability, ease of preparation, wide electrochemical window, low cost, and high design flexibility, which offers the possibility to solve the above-mentioned challenges with ZIBs.[37,38] Compared with the widely used DEEs in lithium batteries, the current research of DEEs for ZIBs is still in its infancy. The major challenge for designing DEEs for ZIBs is the high lattice energy of zinc salt and strong intermolecular interactions between high-charge-density Zn^{2+} and neutral ligands. The high lattice energy of zinc salt potentially causes instability and even crystal precipitation in DEEs. Additionally, the strong intermolecular interactions induce the high viscosity and low ion conductivity of DEEs, which also hinders the practical application of DEEs. Therefore, careful

J. Li, S. Qin, Y. Zhang
State Key Laboratory of Reliability and Intelligence of Electrical Equipment
School of Materials Science and Engineering
Hebei University of Technology
Tianjin 300130, China
E-mail: yongguangzhang@hebut.edu.cn
J. Li, S. Qin, M. Xu, W. Wang, J. Zou, Y. Zhang, H. Dou, Z. Chen
State Key Laboratory of Catalysis
Dalian Institute of Chemical Physics
Chinese Academy of Sciences
Dalian 116023, China
E-mail: haozhen@dicp.ac.cn; zwchen@dicp.ac.cn
The ORCID identification number(s) for the author(s) of this article can be found under https://doi.org/10.1002/adfm.202402186

DOI: 10.1002/adfm.202402186

selection of neutral ligands and regulation of component ratios are required for designing stable DEEs, and three design strategies have been proposed so far. One effective strategy is utilizing the expensive zinc bis(trifluoromethylsulfonyl)imide ($Zn(TFSI)_2$) or hydrated zinc salts. DEEs have been constructed by acetamide and $Zn(TFSI)_2$, and the weak lattice energy of $Zn(TFSI)_2$ facilitates the formation of ionic complexes to obtain stable DEEs. Hydrated zinc salt ($Zn(ClO_4)_2{\cdot}6H_2O$) has been coupled with succinonitrile and methylsulfonylmethane to form DEEs, which exhibit the lowered viscosity and increased ion conductivity arising from the hydration effect.[39,40] Another strategy is the direct addition of bipolar water molecules as a building block for DEEs.[41] However, water is a double-edged sword, the addition of water can improve ion conductivity and interfacial reaction kinetics, but the excessive water content will disrupt the DEE structure and induce side reactions. Therefore, water content needs to be precisely controlled to achieve a dynamic balance between improved Zn^{2+} kinetics and satisfactory reversibility.[42] Recently, organic solvent-neutral ligands have been selected to form DEEs, and the DEEs with $ZnCl_2$-ethylene glycol or $ZnSO_4{\cdot}7H_2O$-propylene glycol configuration are fabricated due to the high solubility of zinc salt in polyhydric alcohol. Although these DEEs demonstrate the distinct advantages of improving cycling stability, the electrochemical performances still need to be optimized and the high concentration of organic solvent poses a potential security risk. Therefore, developing a new design strategy for DEEs is highly needed for the development of high-performance ZIBs.

Herein, supporting salt strategy is proposed for developing multifunctional DEEs without active H_2O, and a novel type of dual-metal-salt derived ternary eutectic electrolytes (DMEEs) are fabricated by integrating zinc trifluoromethylsulfonate ($Zn(OTF)_2$), supporting salt of lithium bis(trifluoromethanesulphonyl)imide (LITFSI) and neutral ligand of N-methyl acetamide (NMA). The introduction of supporting salt with weak lattice energy not only contributes to the formation of stable DMEEs but also endows DMEEs with a wide operating temperature and electrochemical window. Moreover, the supporting salt significantly tailors the Zn^{2+} solvation structure, while the Li^+ competes with Zn^{2+} for the neutral ligand and donates $TFSI^-$ to the Zn^{2+} solvation shell, thus forming dual-anion Zn^{2+} solvation structure. More importantly, the dual-anion solvation structure induces the in situ formation of the inorganic-rich hybrid solid electrolyte interface (SEI) due to the electrochemical decomposition of anions and neutral ligands before Zn deposition. The synergistic effect of the dual-anion solvation shell and in-situ hybrid SEI eliminates HER and corrosion, as well as guides uniform Zn deposition. Remarkably, Zn//Zn symmetrical cell demonstrates a highly reversible Zn^{2+} plating/stripping for over 3000 h, and a full cell paired with a polyaniline (PANI) cathode shows no significant capacity decay after 5000 cycles at a current density of 5 A g^{-1} with a coulombic efficiency close to 100%. The supporting salt strategy opens a new avenue to design advanced eutectic electrolytes, and the deep understanding of Zn^{2+} solvation structure and SEI offers guidelines for developing high-performance batteries.

2. Results and Discussion

2.1. Electrolyte Design and Intermolecular Interactions

DMEEs were fabricated by mixing LITFSI, $Zn(OTF)_2$, and NMA in specific molar ratios. NMA proves to be a favorable ligand for DEEs due to its dipolar nature arising from two polar functional groups of C=O and —NH.[43] This dipolar nature enables the effective coordination with both cation and anion of metal salt. Compared to other amide ligands (such as urea, thiourea, and acetamide), the introduction of a methyl group on the amino in NMA effectively disrupts intramolecular hydrogen bond interactions, resulting in lower viscosity of the prepared DEEs. However, DEE formed by $Zn(OTF)_2$ and NMA was unstable and solidified after 2 h at room temperature (Figure S1, Supporting Information) due to the strong intermolecular interactions. Therefore, a supporting salt strategy is proposed to obtain stable DEEs for ZIBs. LITFSI is selected as the supporting salt due to its weak lattice energy, where the large-sized and electron-delocalized TFSI has lower electrostatic interaction with metal ions compared to OTF, and Li^+ exhibits lower cation–dipole interactions with NMA ligand, thus significantly weakening the intermolecular interactions.[40] Moreover, compared with previously reported DEEs constructed by $Zn(TFSI)_2$, LITFSI exhibits a much lower price (less than a quarter of $Zn(TFSI)_2$, Table S1, Supporting Information), enhancing the economic feasibility of DMEEs. The fabrication of DMEEs was shown in **Figure 1a**, and mixing solid lithium salt, zinc salt, and NMA ligand at the desired molar ratio of 2:1:9 (1:2:9 or 1:1:12) formed the homogeneous liquid DMEE, abbreviated as DMEE219, DMEE129, or DMEE1112. DMEEs were very stable due to the newly formed weak intermolecular interactions and maintained the homogeneous liquid state with no precipitation even after 1 month of storage (Figure S2, Supporting Information), demonstrating that our strategy broadened the scope of DEEs and was also an effective method to regulate the electrolyte structure.

DMEEs exhibited fascinating physical properties compared with the baseline electrolyte of 2 M $Zn(OTF)_2$ aqueous electrolyte (abbreviated as ZF). As revealed by linear sweep voltammetry (LSV) tests (Figure S3, Supporting Information), DMEEs exhibited a more negative overpotential compared to the ZF electrolyte, suggesting the suppressed HER in DMEEs due to the absence of thermodynamically active H_2O. Simultaneously, the oxygen evolution reaction was also inhibited by DMEEs, as evidenced by the increased OER overpotential. Moreover, DMEEs had much lower volatility than of ZF, and the weight loss of DMEEs was only ≈2% after the volatility test in a 60 °C drying oven for 12 h, whereas ZF exhibited a weight loss of up to 32.67% (Table S2 and Figure S4, Supporting Information). Figure S5 (Supporting Information) reflected the freeze-resistance property of DMEEs, and ZF was frozen at −30 °C, while DMEEs could withstand −50 °C ultra-low temperature. Therefore, DMEEs offered a wider working temperature range from −50 °C to +60 °C and demonstrated the better temperature-adaptability of DMEEs than that of ZF.

Intermolecular interactions of DMEEs were investigated by Fourier Transform infrared spectroscopy (FTIR), ^1H nuclear magnetic resonance spectra (^1H NMR), and Raman spectroscopy.

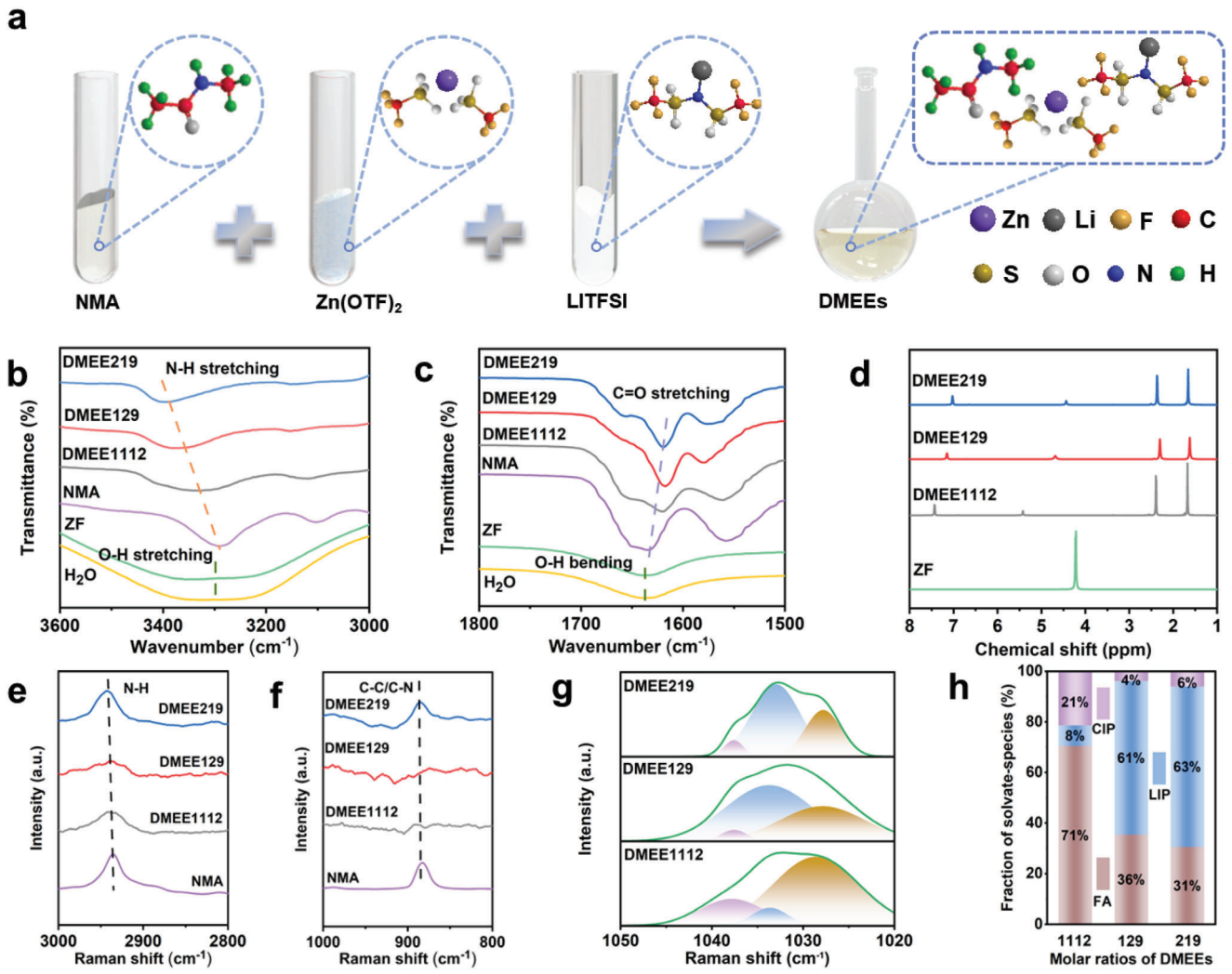

Figure 1. Design of DMEEs and characterizations of intermolecular interactions. a) Schematic diagram of the preparation of DMEEs. b) FTIR spectra of the O—H stretching mode and N-H stretching mode. c) FTIR spectra of the O—H bending mode and C=O stretching mode. d) ^{1}H NMR spectra. e–g) Raman spectra of the DMEEs. h) Solvate species distribution obtained from the fitted Raman spectra in DMEEs (free anions (FA), loose ion pairs (LIP), and contact ion pairs (CIP)).

In the FTIR spectra (Figure 1b,c), the peaks at 3319 and at 1638 cm^{-1} were attributed to the O—H stretching mode and bending mode of H_2O, respectively. When $Zn(OTF)_2$ was added to H_2O to form the ZF electrolyte, the O—H stretching mode shifted to 3356 cm^{-1}, which indicated the strong interactions between Zn^{2+} and H_2O, thus increasing the thermodynamic activity of water and inducing HER reaction. As for NMA, the N-H symmetric stretching vibration peak occurred at 3291 cm^{-1}. After adding metal salts, the peak shifted to 3340 cm^{-1} in the DMEE1112, indicating the breakage of intermolecular hydrogen bond interactions among NMA molecules. Similarly, as the metal salt (zinc salt or lithium salt) content further increased, the peak continued to shift to 3380 and 3395 cm^{-1} in the DMEE129 and DMEE219, confirming the further disruption of hydrogen bond interactions. Meanwhile, the peak at 1635 cm^{-1} in the NMA spectrum was assigned to the C=O stretching vibration, which shifted to 1620 cm^{-1} in the DMEE1112, indicating strong cation–dipole interactions between metal cation (Zn^{2+} and Li^{+}) and NMA due to the solvation of zinc salt or lithium salt by NMA molecules. The O atom of the C=O donor group of NMA possessed high electron cloud density and strongly coordinated with metal cations, which weakened the electrostatic interactions between metal cation (Zn^{2+} or Li^{+}) and anion (OTF or TFSI). As the concentration of metal salt increased, the C=O stretching vibration exhibited a larger blue shift and was located at 1619 cm^{-1} for DMEE219 and 1617 cm^{-1} for DMEE129, which indicated that more interactions occurred between Li^{+} and C=O or between Zn^{2+} and C=O. The largest blue shift of DMEE129 suggested that the interactions between Zn^{2+} and C=O were stronger than those between Li^{+} and C=O due to the high charge of Zn^{2+}. ^{1}H NMR spectra were also performed to understand the hydrogen bond interactions. As shown in Figure 1d, the chemical shift of NH of NMA appeared at 7.43 ppm, and the chemical shifts of CH_3 occurred at 1.68 and 2.40 ppm in the DMEE1112 electrolyte. The chemical shift of NH of NMA moved to 7.15 ppm for DMEE129 and 7.02 ppm for DMEE219, and the up-filed shift indicated the destruction of the

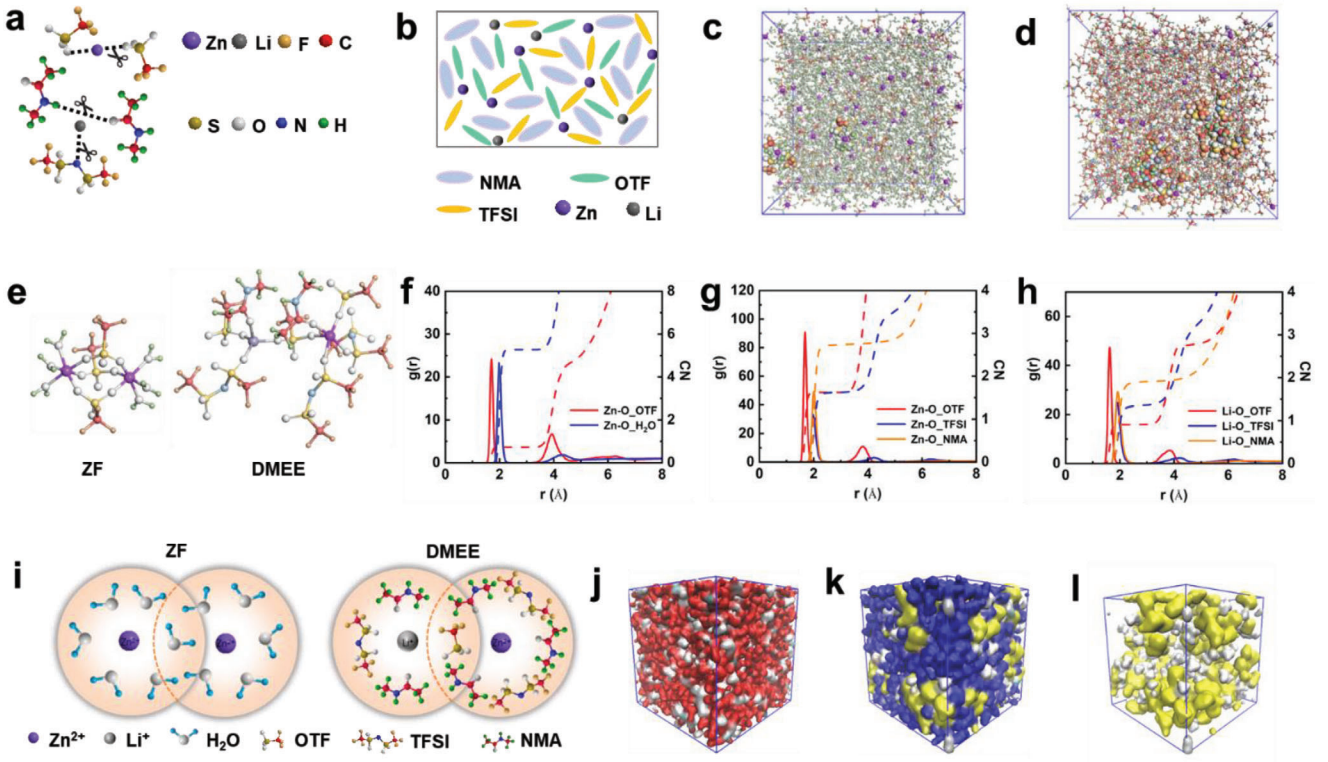

Figure 2. Formation mechanism of DMEEs and Zn^{2+} solvation structure. a) Breakage of ionic bonds and hydrogen bonds during the formation of DMEEs. b) Solvation of Zn^{2+} and Li^{+} by NMA molecules and ion aggregates in DMEEs. c,d) Snapshots of MD simulations for ZF and DMEE219, color bar: grey Li, red C, orange F, yellow S, white O, purple Zn, blue N, green H. e) Enlarged Zn^{2+} solvation structure extracted from MD simulations. f–h) RDF g(r) and coordination number N(r) of ZF and DMEE219. i) Average Zn^{2+} solvation structure in ZF and DMEE219. j–l) Ion and molecule aggregation distribution of ZF and DMEE219, color bar: red H_2O, white OTF, yellow TFSI, and blue NMA.

original hydrogen bond network among NMA molecules enabled by the addition of more zinc salt or lithium salt. As shown in Raman spectra (Figure 1e,f), the symmetric stretching peak of N—H was located at 2936 cm^{-1} in the NMA and exhibited different blue shifts in the DMEEs, and the stretching vibration peak of C—N also underwent the slight blue shifts in the DMEEs due to the strong interactions between C=O and metal cation, being consistent with the FTIR results. Furthermore, stretching vibration peaks of OTF and TFSI in the DMEE129 and DMEE219 moved to higher wavenumber compared with DMEE1112, which suggested the formation of more contact ion pairs and ion aggregates with the addition of more metal salt, demonstrating the participation of OTF or TFSI into the Zn^{2+} solvation shell (Figure 1g,h). Based on the above spectroscopy characterization, the formation mechanism of DMEEs is elaborated. Mixing NMA and metal salt effectively eliminated the intramolecular hydrogen bond interactions of NMA and weakened the cation-anion electrostatic interactions (**Figure** 2a). Meanwhile, the strong cation-dipole interactions between the metal cation and C=O resulted in the weakend hydrogen bond interactions in NMA molecules and the solvation or insertion of metal salt by NMA molecules, which contributed to the dissociation of metal salt and generated more ion pairs and ion aggregates, thus delocalizing the charge of both cation and anion and generating the homogeneous and stable DMEEs (Figure 2b).

2.2. Solvation Structure of DMEEs

The solvation structure of ZF and DMEE was investigated by molecular dynamics (MD) simulations and density functional theory (DFT) calculations. As seen from snapshots and splitting of MD simulations, the bulk structure of DMEE underwent significant changes compared with ZF. In ZF, Zn^{2+} and OTF were surrounded by abundant H_2O molecules with uniform distribution (Figure 2c; Figure S6, Supporting Information). In DMEE, the introduction of LITFSI brought more possibilities for the solvation shell, lithium salt provided TFSI anions for the Zn^{2+}solvation shell, and the OTF anions from $Zn(OTF)_2$ also enriched the Li^{+} solvation shell, while the neutral ligand NMA participated in the both Li^{+} and Zn^{2+} solvation shell (Figure 2d; Figure S7, Supporting Information). The typical ionic and molecular microenvironment ≈2 adjacent metal cations were extracted from MD simulations, which further highlighted the different solvation structures in ZF and DMEE (Figure 2e). In ZF, two adjacent Zn^{2+} cations coordinated with 6 H_2O molecules and 3 OTF anions, while the adjacent Zn^{2+} and Li^{+} were solvated by 2 NMA molecules, 5 OTF anions, and 3 TFSI anions in DMEE, demonstrating the effective modulation of solvation structures by addition of lithium salt.

Radial distribution function (RDF) and coordination number (CN) were applied to reveal the Zn^{2+} solvation shell

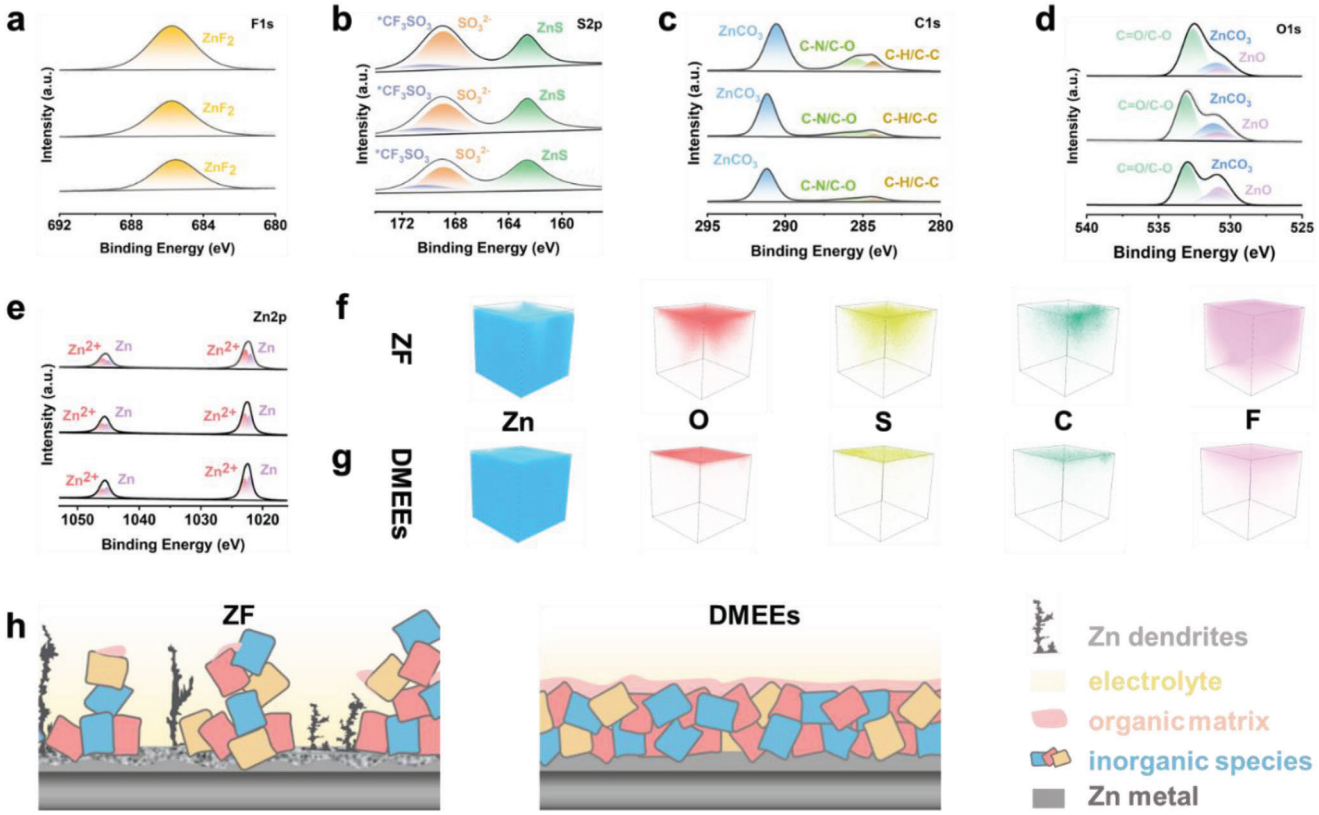

Figure 3. Interface chemistry. a–e) XPS spectra of Zn anode after 30 cycles in DMEEs with in-depth profiles at Ar^+ sputtering time of 0, 180, and 600 s (from up to bottom): F1s (a), S2p (b), C1s (c), O1s (d), and Zn2p (e). f,g) 3D views of element distribution in the sputtering volume of TOF-SIMS for ZF (f) and DMEEs (g). h) Dendrites and side reactions on the Zn anode in ZF and SEI of Zn anode in DMEEs.

quantificationally. The H_2O-Zn^{2+} RDF in ZF indicated the coordination peak at 1.975 Å with a CN of 5.27, while Zn^{2+}-OTF RDF showed the coordination peak at 1.725 Å with a CN of 0.73, which suggested Zn^{2+} primary solvation shell was composed of 5.27 H_2O molecules and 0.73 OTF anion on average (Figure 2f). As shown in Figure 2g, the Zn^{2+}-NMA, Zn^{2+}-OTF, and Zn^{2+}-TFSI coordination peaks were located at 2.025, 1.675, and 1.975 Å with the CN of 2.74, 1.63, 1.63, respectively, demonstrating a significant change in Zn^{2+}solvation structure in DMEE. Additionally, as revealed by RDF and CN, the Li^+-NMA, Li^+-OTF, and Li^+-TFSI coordination peaks occurred at 1.925, 1.625, and 1.925 Å, and Li^+ formed a solvation shell with 1.91 NMA, 0.92 OTF, and 1.36 TFSI (Figure 2h). As highlighted by CN of Zn^{2+} and Li^+, the addition of lithium salt provided Zn^{2+} with TFSI anion, while the dissociated Li^+ competed with Zn^{2+} for NMA neutral ligands. Figure 2i presents the average Zn^{2+} solvation structures of ZF and DMEEs. ZF possessed a water-rich solvation structure, which generated abundant active H_2O, thus accelerating parasitic reactions such as HER and corrosion. In contrast, DMEEs possessed dual-anion-rich solvation structure, thereby avoiding parasitic reactions and being likely to induce the anion-dominated interface chemistry.

Molecular dynamics simulations were also performed to gain insight of the nanostructure and the related component aggregation of DMEEs (Figures 2j–l). In ZF, the OTF anions were discretely dispersed in the continuous phase of aggregated H_2O molecules (Figure 2j; Figure S8, Supporting Information). However, in DMEEs, OTF and TFSI anions started to aggregate into a continuous phase, which interpenetrated with the continuous phase of aggregated NMA molecules, thus forming the bicontinuous nanostructure (Figure 2k,l; Figure S9, Supporting Information). Furthermore, the free energy of two adjacent solvated metal cations of ZF and DMEEs was calculated by DFT calculation (Figure S10, Supporting Information). The free energy of two adjacent solvated Zn^{2+} was 72.73 eV in ZF, while the free energy of two adjacent solvated Zn^{2+} and Li^+ was 63.70 eV. The lower free energy will contribute to the fast desolvation process during Zn^{2+} plating.

2.3. SEI Chemistry and Structure of Zn Anode

Interface chemistry of Zn anodes after 30 cycles in ZF and DMEE was characterized by X-ray photoelectron spectroscopy (XPS) and time-of-flight secondary ion mass spectrometry (TOF-SIMS). The XPS survey spectra confirmed the higher F content of Zn anode in DMEEs in comparison to ZF (Figure S11, Supporting Information). In the F1s spectra (**Figure** 3a; Figure S12a, Supporting Information), the peak at 685.7 eV was assigned to inorganic ZnF_2, which originated from the electrochemical decomposition of OTF or TFSI. ZnF_2 content of the Zn anode in DMEEs was significantly higher than that in ZF at different sputtering

times due to the dual-anion-rich solvation structure. In the S2p spectra (Figure 3b; Figure S12b, Supporting Information), ZnS (162.6 eV), $ZnSO_3$ (168.9 eV), and organic S (170.4 eV) could be observed, inorganic ZnS and $ZnSO_3$ were the dominated components of Zn anode in DMEEs, while the organic S component from OTF exhibited much higher content in ZF due to the side reactions. In the C1s spectra (Figure 3c; Figure S12c, Supporting Information), three signal peaks at 284.3, 285.4, and 290.5 eV were ascribed to C—H/C—C, C—N/C—O, and $ZnCO_3$, which further highlighted the electrochemical decomposition of OTF in both ZF and DMEEs. Organic carbon components were much higher than $ZnCO_3$ in ZF, while $ZnCO_3$ was the main component of Zn anode in DMEEs, which could still be detected after 600 s sputtering. In the O1s spectra (Figure 3d; Figure S12d, Supporting Information), Zn anode in ZF presented three components of S—O (532.7 eV), $ZnCO_3$ (531.1 eV), and $Zn(OH)_2$ (530.5 eV), and the high content of S—O and $Zn(OH)_2$ indicated the irreversible side reactions, which hindered the formation of stable SEI in ZF. While SEI of Zn anode in DMEEs comprised a high content of C=O component, which was attributed to the electrochemical decomposition of NMA. Moreover, the favorable inorganic component of ZnO (530.8 eV) was formed in DMEEs. Zn2p spectra indicated a significantly higher Zn^{2+}content on Zn anode surface of DMEEs, suggesting that large amounts of zinc compounds gathered on the surface of Zn anode and contributed to the formation of dense SEI (Figure 3e; Figure S12e, Supporting Information). Moreover, the N1s peak at 399.4 eV can be attributed to organic N—C species originating from TFSI,[44,45] while the Li1s peak at 55.6 eV corresponds to Li—F and the peak at 56.4 eV corresponds to Li—O.[45,46] N1s and Li1s spectra highlighted the addition of lithium could tailor the interface chemistry of Zn anode in DMEEs (Figure S13, Supporting Information).

The element and compound distribution in the SEI was further studied using TOF-SIMS. As shown in Figure 3f,g, compared to ZF, the Zn anode in DMEEs exhibited an even and dense Zn plating with no visible craters, and all elements were distributed only in the surface layer, indicating a uniform SEI structure. Similar results were confirmed from the distribution of various compounds (Figure S14, Supporting Information). The normalized depth profiles of TOF-SIMS (Figure S15, Supporting Information) showed the ever-increasing Zn element with the prolonging of the sputtering time, indicating the unstable interface chemistry of Zn anode in the ZF. In contrast, Zn element of Zn anode in DMEEs witnessed a rapid increase and reached the stable content after 200 s, and the content of other elements also experienced a rapid increase and then a rapid decrease with approaching zero, which further suggested the formation of a uniform SEI layer. As illustrated in Figure 3h, the Zn anode in ZF suffered from severe corrosion and dendrite growth, and the generated compounds such as ZnF_2 and ZnS were discretely distributed on the Zn anode. While an inorganic-rich hybrid SEI containing ZnF_2, ZnS, $ZnSO_3$, $ZnCO_3$, ZnO, and organic components was in-situ constructed in DMEEs due to the more decomposition of anions and NMA induced by the dual-anion solvation structure of DMEEs, which suppressed side reactions and manipulated the uniform Zn^{2+} deposition to obtain highly reversible Zn anode.

2.4. Structural Evolution of Zn Anode

The structural evolution of Zn anodes in ZF and DMEEs was investigated by multiple characterizations. As seen from scanning electron microscope (SEM) images, Zn anode after immersion in ZF for 14 days was covered with irregular sheet-like by-products (Figure S16, Supporting Information), indicating the continuous corrosion reactions. In contrast, Zn anode immersed in DMEEs maintained its original smooth surface, which suggested the DMEEs electrolyte effectively prevented the chemical corrosion of Zn anode. The morphology of Zn anode after different cycles in ZF and DMEEs was analyzed by SEM (Figure S17, Supporting Information). Zn anode surface in ZF after 10 cycles exhibited noticeable zinc dendrites with disorderly arrangement and a tendency for vertical growth (**Figure** 4a). After 30 cycles, sheet-like dendrites continued to grow in size (Figure 4b). It could be foreseen that if the battery continued to work, the zinc dendrites would continue to grow, eventually puncturing the separator and leading to a short circuit. In addition, small cracks were observed on the Zn anode surface, which was not conducive to the long-term cycling of Zn anode. It was noteworthy that Zn anode exhibited a regular layer-like deposition with a dense and uniform structure after ten cycles in DMEEs (Figure 4c). Even after 30 cycles, Zn anode remained layered morphology with intact and clear texture, indicating that the DMEEs electrolyte significantly suppressed side reactions and regulated the deposition morphology of Zn anode (Figure 4d). The cross-section morphology of Zn anodes after 30 cycles was obtained using a focused ion beam-scanning electron microscope (FIB-SEM). As shown in Figure 4e,f, Zn anode cycled in ZF exhibited an uneven deposition morphology with an irregular porous structure, which resulted in the rapid volume expansion of Zn anode and increased contact area between the fresh Zn anode and the electrolyte, eventually accelerating the uncontrolled side reactions. In contrast, Zn anode in DMEEs obtained a uniform and dense structure with a high stacking density, significantly improving the reversibility of Zn anode (Figure 4g,h). X-ray diffraction (XRD) was used to analyze the crystal structure and orientation of Zn anode. As shown in Figure 4i, (002) crystal plane (36°) of Zn anode significantly increased in DMEEs after 30 cycles compared to ZF, which indicated DMEEs promoted the oriented growth of Zn along the (002) plane, thereby suppressing the growth of zinc dendrites. Meanwhile, no significant peak of by-products was observed, indicating that the DMEEs could suppress the generation of by-products. In contrast, in the XRD pattern of the Zn anode cycled in ZF, clear peaks of the by-product $Zn_x(OTF)_y(OH)_{2x-y}{\cdot}nH_2O$ were observed, which led to abnormal consumption of Zn anode.

Encouraged by the morphology regulation of Zn anode by DMEEs, cyclic voltammetry (CV) and chronoamperometry (CA) curves of Zn//Ti cells were measured to further investigate the initial nucleation and Zn^{2+} diffusion behavior. Compared to ZF, the nucleation overpotential of DMEEs obviously increased, resulting in a decrease in nucleation radius and an increase in nucleation quality, which was beneficial for even Zn^{2+} deposition (Figure 4j). The nucleation behaviors in ZF and DMEEs were captured by SEM characterization (Figure S18,

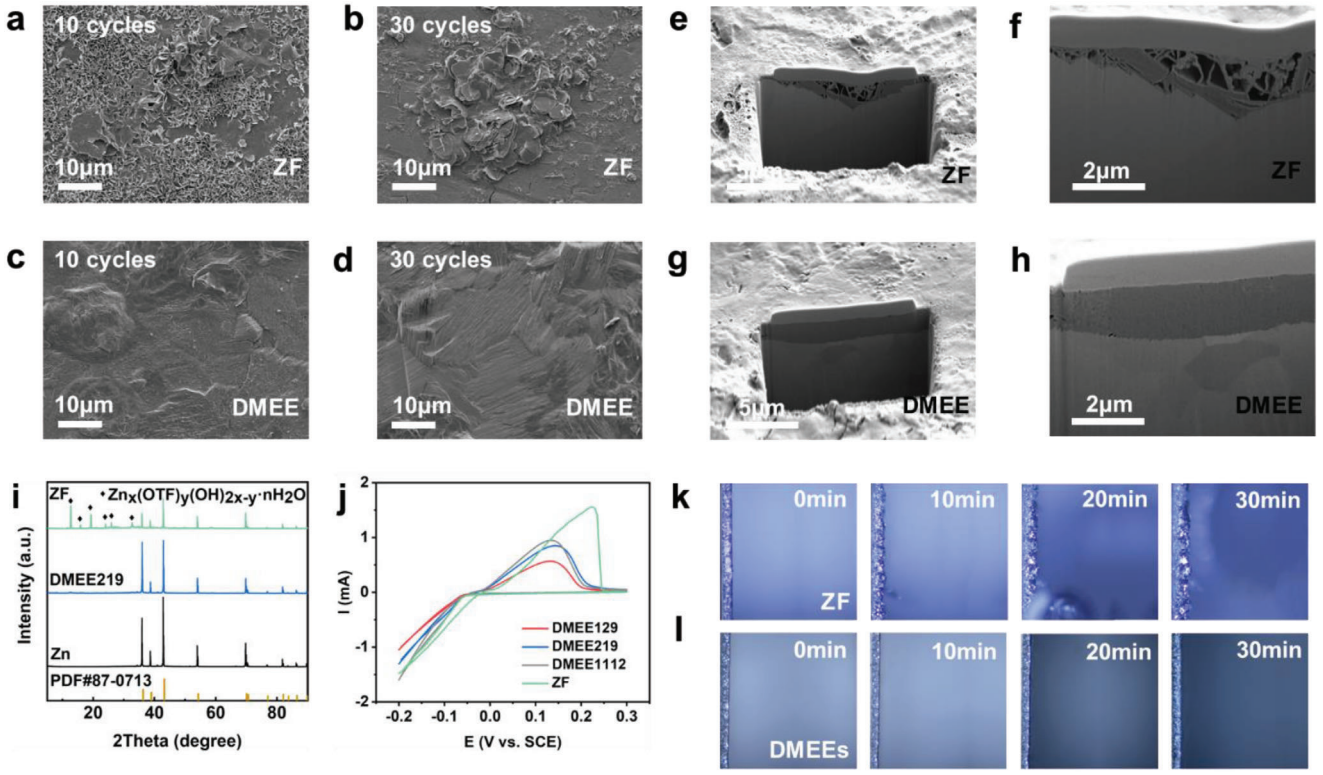

Figure 4. Structural evolution of Zn anodes in ZF and DMEEs. a–d) SEM images of Zn anodes cycled in ZF a,b) and DMEE c,d) for ten cycles and 30 cycles. e–h) Cross-sectional morphology of Zn anodes captured by FIB after 30 cycles in ZF e,f) and DMEE g,h). i) XRD patterns of Zn anodes after 30 cycles in ZF and DMEE. j) CV curves of Zn//Ti cells in ZF and DMEE at 1 mVs^{-1}. k,l) In situ optical microscopy characterization of Zn deposition in ZF and DMEE.

Supporting Information). Within 12 min of Zn^{2+} deposition in ZF, Zn anode exhibited nonuniform nucleation and dendrite growth, starting from bits of crystal nuclei and fragmented protrusions, and ending up large-sized dendrites. In contrast, the number of nuclei increased and their size decreased for Zn anode in DMEEs, contributing to the dense and smooth deposition. Additionally, Zn^{2+} diffusion was investigated through CA tests (Figure S19, Supporting Information). In ZF, the current density exhibited a continuous increase within 300 s, indicating prolonged and extensive 2D diffusion. In contrast, a stable 3D diffusion was established after 50-s 2D diffusion in DMEEs, indicating the uniform Zn^{2+} diffusion and even deposition, as evidenced by the stable and significantly reduced current density. Therefore, DMEEs could regulate the Zn nucleation and induce Zn^{2+} uniform deposition to obtain a dendrite-free Zn anode.

In situ optical microscopy was performed to visualize the Zn^{2+} deposition at 1 mA cm^{-2} for 30 min. Zn^{2+} preferentially deposited on the initially protruding tips and continued to grow in the same position accompanied by the evolution of gas bubbles in ZF, which suggested the severe dendrite growth and HER (Figure 4k). In sharp contrast, Zn deposition in DMEEs maintained the dense and uniform morphology without gas evolution, further validating the effectiveness of DMEEs in regulating Zn^{2+} deposition behavior to promote high reversibility of Zn anode (Figure 4l).

2.5. Electrochemical Performance

Cycling stability and coulombic efficiency (CE) of Zn stripping/plating with DMEEs were investigated by using Zn//Zn and Zn//Cu cells. Zn//Zn cell employing ZF exhibited stable operation for only 120 h (Figure S20, Supporting Information), and the cell voltage suddenly dropped with losing the charge and discharge peaks due to the internal short circuits caused by dendrite penetration. In contrast, Zn//Zn cells with DMEEs exhibited a significantly prolonged lifetime with stable polarization values below 70 mV (Figure S21, Supporting Information). Both DMEE1112 and DMEE129 afforded the cycling stability of 600 and 700 h. Especially, Zn//Zn cells using DMEE219 electrolyte demonstrated cycling stability for over 2600 h at 0.1 mA cm^{-2} and 0.1 mAh cm^{-2}, which was 20 times higher than that of ZF. Therefore, DMEE219 electrolyte was used as a representative for the subsequent battery measurements. Remarkably, upon elevating the current density to 0.5 mA cm^{-2}, DMEEs could extend the cycling life of Zn//Zn beyond 3000 h with stable voltage-time curves (**Figure 5a**; Figure S22, Supporting Information), outperforming many previously reported Zn//Zn batteries based on eutectic electrolytes and highly concentrated electrolytes (Table S3, Supporting Information).[39,40,47–49] Zn//Zn cells utilizing DMEEs consistently demonstrated stable voltage polarization at the elevated current density from 0.1 to 0.5 mA cm^{-2}. More impressively, when the current density was

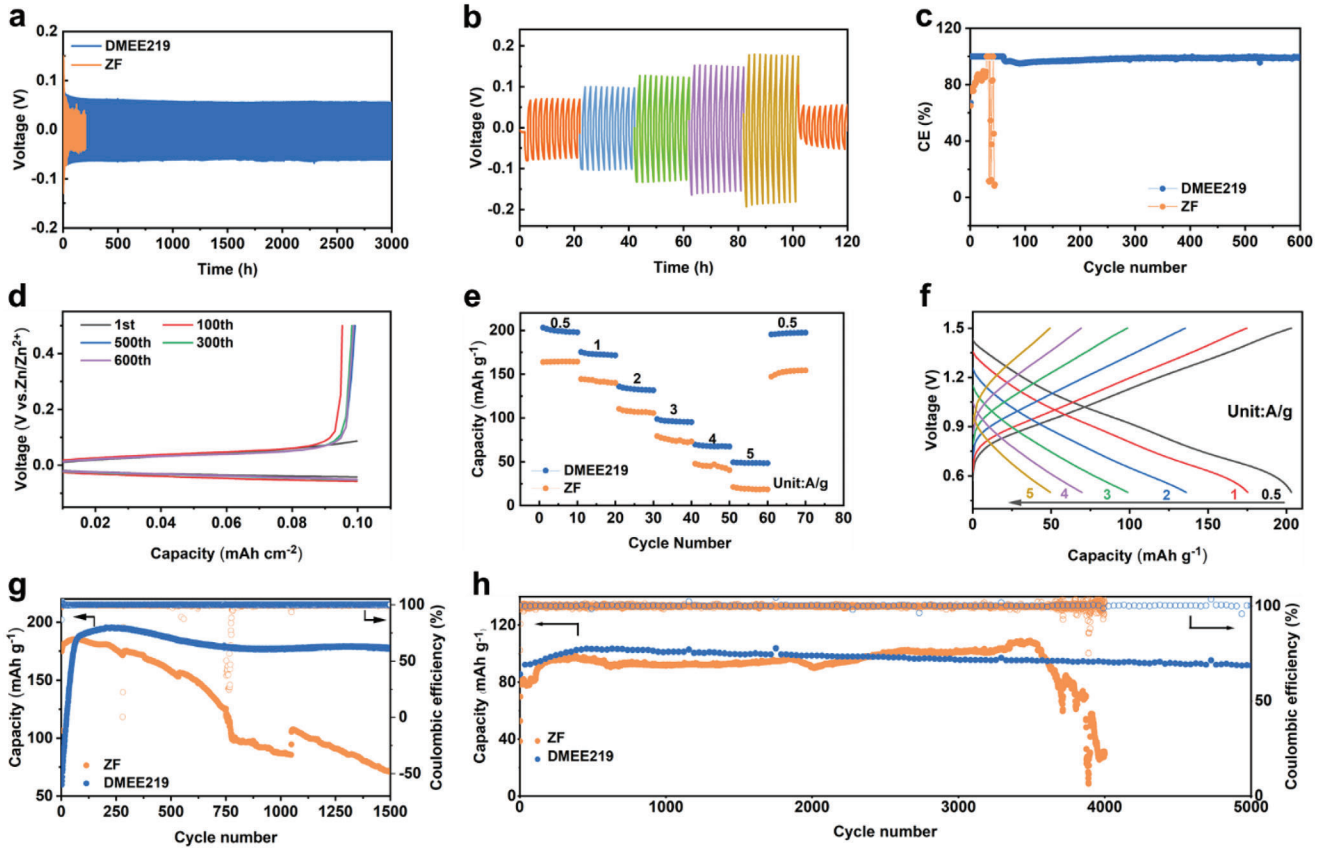

Figure 5. Electrochemical performance. a) Cyclic performance of Zn//Zn cells using ZF and DMEEs with 0.5 mA cm^{-2} and 0.1 mAh cm^{-2}. b) Rate performance at the fixed 1 h charge/discharge time under current densities of 0.1, 0.2, 0.3, 0.4, and 0.5 mA cm^{-2} with DMEEs. c) CE curves of Zn//Cu cells in ZF and DMEEs at 0.1 mA cm^{-2} and 0.1 mAh cm^{-2}. d) Capacity-voltage curves of Zn//Cu cells with DMEEs at 0.1 mA cm^{-2} and 0.1 mAh cm^{-2}. e) Rate performance of Zn//PANI full cells using ZF and DMEEs. f) Discharge/charge voltage curves of Zn//PANI full cell with DMEEs. g) Cycling performance of Zn//PANI full cell at 1 A g^{-1}. h) Cycling performance of Zn//PANI full cell at 5 A g^{-1}.

recovered to 0.1 mA cm^{-2}, the cell continued to operate normally with almost 100% voltage recovery, further underscoring the exceptional rate performance (Figure 5b). Furthermore, Zn//Zn cells with DMEEs could stably operate at a high current density of 1 mA cm^{-2}, as evidenced by the stable voltage-time curve (Figure S23, Supporting Information). The significantly improved cycling stability of Zn//Zn cells mainly lies in the dual-anion-rich Zn^{2+} solvation shell and inorganic-rich hybrid in situ SEI.

CE of Zn anode with ZF and DMEEs was further studied by Zn//Cu cells. As revealed in Figure 5c, CE of the Zn//Cu cell with ZF exhibited irregular fluctuations with an average value of 83.2% during the initial 30 cycles and quickly dropped to zero after 40 cycles. In contrast, Zn//Cu cell provided cycling stability for over 600 cycles, and a high and stable CE of over 98.4% during the initial 100 cycles was obtained, which increased up to 99.3% for the final 100 cycles. As highlighted by capacity-voltage curves (Figure 5d; Figure S24, Supporting Information), ZF delivered unstable voltage curves while the stable charge/discharge curves and acceptable polarization (≈86 mV) were achieved in DMEEs.

Zn//PANI (polyaniline) full cells were employed to verify the practical applicability of DMEEs. The electrochemical behavior of PANI in DMEEs was understood by CV curves (Figure S25, Supporting Information). CV curves exhibited two sets of reversible redox peaks and overlapped well in two cycles with no significant decrease in peak current, indicating the high stability and reversibility of PANI cathode in the DMEEs. The excellent rate performance of Zn//PANI cell was achieved by DMEEs (Figure 5e), which exhibited a high and stable specific capacity at all current densities from 0.5 to 5 A g^{-1}. Upon reverting the current density to 0.5 A g^{-1}, the capacity rebounded to 195.5 mAh g^{-1}, showcasing the fast interface reaction kinetics. The corresponding charge/discharge curves at different current densities are shown in Figure 5f. The cycling performance of Zn//PANI full cells with ZF and DMEEs at 1 A g^{-1} was shown in Figure 5g. The capacity of full cells with ZF rapidly declined in the initial stage and witnessed severe fluctuations after 700 cycles, followed by cell failure. In contrast, the full cell with DMEEs exhibited a capacity of 177.2 mAh g^{-1} after 1500 cycles with a capacity retention of 90.6%, demonstrating better reversibility. Additionally, long-term cycling stability of Zn//PANI full cells was also obtained at a high current density of 5 A g^{-1} (Figure 5h), further demonstrating the superiority of DMEEs. Notably, even after 5000 cycles, the battery maintained a specific capacity of 91.7 mAh g^{-1} with a capacity retention of 88.5%, and the coulombic efficiency remained close to 100%. The excellent electrochemical performance of Zn//PANI

full cells demonstrated the great potential of DMEEs for practical application.

3. Conclusion

In conclusion, we proposed a novel supporting salt strategy to design multifunctional DMEEs for highly reversible ZIBs. DMEEs were constructed by $Zn(OTF)_2$, supporting salt of LITFSI, and neutral ligand of NMA, which showed a wider operating temperature and electrochemical window compared with ZF. The introduction of LITFSI with weak lattice energy disrupted the hydrogen bond interactions among NMA molecules, induced more cation–dipole interactions, and weakened cation-anion electrostatic interactions, which contributed to the formation of ion pairs and ion aggregates, thus generating the homogeneous and stable DMEEs. Moreover, the addition of lithium salt provided Zn^{2+} with TFSI anion, while the dissociated Li^+ competed with Zn^{2+} for NMA neutral ligands, thus endowing the DMEEs with a dual-anion rich solvation shell. More importantly, inorganic-rich SEI was in-situ constructed by the electrochemical decomposition of anions and NMA, which suppressed side reactions and afforded dendrite-free Zn anode due to effective regulation of both Zn^{2+} nucleation and diffusion. As a result, the Zn anode delivered high reversibility for over 3000 h, and the Zn//PANI cell maintained commendable capacity retention of 88.5% even after 5000 cycles at a high current density of 5 A g^{-1}. This work had significant implications for developing versatile eutectic electrolytes for high-performance batteries.

Supporting Information

Supporting Information is available from the Wiley Online Library or from the author.

Acknowledgements

The authors thank for the support of the Strategic Priority Research Program of the Chinese Academy of Sciences (XDB0600100). The authors are grateful for the technical support for the Vacuum Interconnected Nanotech Workstation (Nano-X) from Suzhou Institute of Nano-Tech and Nano-Bionics, Chinese Academy of Sciences (SINANO). The authors would like to thank Dr. Rong Huang for the help in TOF-SIMS collection and Dr. Zhiyun Li for conducting the XPS characterizations.

Conflict of Interest

The authors declare no conflict of interest.

Data Availability Statement

The data that support the findings of this study are available from the corresponding author upon reasonable request.

Keywords

eutectic electrolytes, solid electrolyte interface, solvation structure, supporting salt strategy, Zn anode

Received: February 4, 2024
Revised: March 11, 2024
Published online:

[1] X. Zheng, X. Zhao, J. Lu, J. Li, Z. Miao, W. Xu, Y. Deng, A. L. Rogach, *Sci. China Mater.* **2022**, *65*, 2393.
[2] Y. Zhao, S. Guo, M. Chen, B. Lu, X. Zhang, S. Liang, J. Zhou, *Nat. Commun.* **2023**, *14*, 7080.
[3] Y. Wang, Z. Li, W. Xie, Q. Zhang, Z. Hao, C. Zheng, J. Hou, Y. Lu, Z. Yan, Q. Zhao, J. Chen, *Angew. Chem., Int. Ed.* **2023**, *136*, 202310905.
[4] H. Cui, D. Zhang, Z. Wu, J. Zhu, P. Li, C. Li, Y. Hou, R. Zhang, X. Wang, X. Jin, S. Bai, C. Zhi, *Energy Environ. Sci.* **2024**, *17*, 114.
[5] Y. Lyu, J. A. Yuwono, P. Wang, Y. Wang, F. Yang, S. Liu, S. Zhang, B. Wang, K. Davey, J. Mao, Z. Guo, *Angew. Chem., Int. Ed.* **2023**, *62*, 202303011.
[6] H. Dou, M. Xu, Y. Zheng, Z. Li, G. Wen, Z. Zhang, L. Yang, Q. Ma, A. Yu, D. Luo, X. Wang, Z. Chen, *Adv. Mater.* **2022**, *34*, 2110585.
[7] J.-L. Yang, Z. Yu, J. Wu, J. Li, L. Chen, T. Xiao, T. Xiao, D.-Q. Cai, K. Liu, P. Yang, H. J. Fan, *Adv. Mater.* **2023**, *35*, 2306531.
[8] M. Xu, H. Dou, Z. Zhang, Y. Zheng, B. Ren, Q. Ma, G. Wen, D. Luo, A. Yu, L. Zhang, X. Wang, Z. Chen, *Angew. Chem., Int. Ed.* **2022**, *61*, 202117703.
[9] P. Liang, H. Hu, Y. Dong, Z. Wang, K. Liu, G. Ding, F. Cheng, *Adv. Funct. Mater.* **2024**, 2309858.
[10] V. Etacheri, R. Marom, R. Elazari, G. Salitra, D. Aurbach, *Energy Environ. Sci.* **2011**, *4*, 3243.
[11] S. Choi, G. Wang, *Adv. Mater. Technol.* **2018**, *3*, 1700376.
[12] J. Hou, M. Yang, D. Wang, J. Zhang, *Adv. Energy Mater.* **2020**, *10*, 1904152.
[13] C. Sun, X. Ji, S. Weng, R. Li, X. Huang, C. Zhu, X. Xiao, T. Deng, L. Fan, L. Chen, X. Wang, C. Wang, X. Fan, *Adv. Mater.* **2022**, *34*, 2206020.
[14] J. Wang, X. Lei, S. Guo, L. Gu, X. Wang, A. Yu, D. Su, *Renewables* **2023**, *1*, 316.
[15] L. Qian, T. Or, Y. Zheng, M. Li, D. Karim, A. Cui, M. Ahmed, W. P. Hey, Z. Zhang, Y. Deng, A. Yu, Z. Chen, K. Amine, *Renewables* **2023**, *1*, 114.
[16] L. Shen, H. B. Wu, F. Liu, J. Shen, R. Mo, G. Chen, G. Tan, J. Chen, X. Kong, X. Lu, Y. Peng, J. Zhu, G. Wang, Y. Lu, *Adv. Funct. Mater.* **2020**, *30*, 2003055.
[17] Y.-K. Liu, C.-Z. Zhao, J. Du, X.-Q. Zhang, A.-B. Chen, Q. Zhang, *Small* **2023**, *19*, 2205315.
[18] R. Du, Y. Jie, Y. Chen, F. Huang, W. Cai, Y. Liu, X. Li, S. Wang, Z. Lei, R. Cao, G. Zhang, S. Jiao, *ACS Appl. Energy Mater.* **2020**, *3*, 6692.
[19] J. Hao, L. Yuan, Y. Zhu, X. Bai, C. Ye, Y. Jiao, S.-Z. Qiao, *Angew. Chem., Int. Ed.* **2023**, *62*, 202310284.
[20] Q. Ma, R. Gao, Y. Liu, H. Dou, Y. Zheng, T. Or, L. Yang, Q. Li, Q. Cu, R. Feng, Z. Zhang, Y. Nie, B. Ren, D. Luo, X. Wang, A. Yu, Z. Chen, *Adv. Mater.* **2022**, *34*, 2207344.
[21] R. Zhao, X. Dong, P. Liang, H. Li, T. Zhang, W. Zhou, B. Wang, Z. Yang, X. Wang, L. Wang, Z. Sun, F. Bu, Z. Zhao, W. Li, D. Zhao, D. Chao, *Adv. Mater.* **2023**, *35*, 2209288.
[22] Y. Yin, X. Li, *Renewables* **2023**, *1*, 622.
[23] Y. Dong, N. Zhang, Z. Wang, J. Li, Y. Ni, H. Hu, F. Cheng, *J. Energy Chem.* **2023**, *83*, 324.
[24] H. Peng, C. Wang, D. Wang, X. Song, C. Zhang, J. Yang, *Angew. Chem., Int. Ed.* **2023**, *62*, 202308068.
[25] Y. Zeng, Z. Pei, Y. Guo, D. Luan, X. Gu, X. W. Lou, *Angew. Chem., Int. Ed.* **2023**, *62*, 202312145.
[26] R. Wang, M. Yao, M. Yang, J. Zhu, J. Chen, Z. Niu, *PNAS* **2023**, *120*, 2221980120.
[27] F. Bu, Y. Gao, W. Zhao, Q. Cao, Y. Deng, J. Chen, J. Pu, J. Yang, Y. Wang, N. Yang, T. Meng, X. Liu, C. Guan, *Angew. Chem., Int. Ed.* **2024**, *136*, 202318496.
[28] H. Li, Y. Ren, Y. Zhu, J. Tian, X. Sun, C. Sheng, P. He, S. Guo, H. Zhou, *Angew. Chem., Int. Ed.* **2023**, *62*, 202310143.
[29] D. Han, Z. Wang, H. Lu, H. Li, C. Cui, Z. Zhang, R. Sun, C. Geng, Q. Liang, X. Guo, Y. Mo, X. Zhi, F. Kang, Z. Weng, Q.-H. Yang, *Adv. Energy Mater.* **2022**, *12*, 2102982.

[30] B. Liu, S. Wang, Z. Wang, H. Lei, Z. Chen, W. Mai, *Small* **2020**, *16*, 2001323.
[31] S.-B. Wang, Q. Ran, R.-Q. Yao, H. Shi, Z. Wen, M. Zhao, X.-Y. Lang, Q. Jiang, *Nat. Commun.* **2020**, *11*, 1634.
[32] Q. Zhang, J. Luan, X. Huang, Q. Wang, D. Sun, Y. Tang, X. Ji, H. Wang, *Nat. Commun.* **2020**, *11*, 3961.
[33] L. Dai, T. Wang, B. Jin, N. Liu, Y. Niu, W. Meng, Z. Gao, X. Wu, L. Wang, Z. He, *Surf. Coat. Technol.* **2021**, *427*, 127813.
[34] M. A. Dzhavakhyan, Y. E. Prozhogina, *Pharm. Chem. J.* **2023**, *57*, 296.
[35] F. M. Perna, P. Vitale, V. Capriati, *Curr. Opin. Green Sustainable Chem.* **2020**, *21*, 27.
[36] Q. Zhang, K. De Oliveira Vigier, S. Royer, F. Jérôme, *Chem. Soc. Rev.* **2012**, *41*, 7108.
[37] E. S. C. Ferreira, C. M. Pereira, A. F. Silva, *J. Electroanal. Chem.* **2013**, *707*, 52.
[38] A. P. Abbott, G. Capper, K. J. McKenzie, A. Glidle, K. S. Ryder, *Phys. Chem. Chem. Phys.* **2006**, *8*, 4214.
[39] H. Qiu, X. Du, J. Zhao, Y. Wang, J. Ju, Z. Chen, Z. Hu, D. Yan, X. Zhou, G. Cui, *Nat. Commun.* **2019**, *10*, 5374.
[40] W. Yang, X. Du, J. Zhao, Z. Chen, J. Li, J. Xie, Y. Zhang, Z. Cui, Q. Kong, Z. Zhao, C. Wang, Q. Zhang, G. Cui, *Joule* **2020**, *4*, 1557.
[41] M. Li, X. Wang, J. Hu, J. Zhu, C. Niu, H. Zhang, C. Li, B. Wu, C. Han, L. Mai, *Angew. Chem., Int. Ed.* **2023**, *62*, 202215552.
[42] R. Chen, C. Zhang, J. Li, Z. Du, F. Guo, W. Zhang, Y. Dai, W. Zong, X. Gao, J. Zhu, Y. Zhao, X. Wang, G. He, *Energy Environ. Sci.* **2023**, *16*, 2540.
[43] A. Boisset, J. Jacquemin, M. Anouti, *Electrochim. Acta* **2013**, *102*, 120.
[44] D. Li, L. Cao, T. Deng, S. Liu, C. Wang, *Angew. Chem., Int. Ed.* **2021**, *60*, 13035.
[45] W. Yu, Z. Yu, Y. Cui, Z. Bao, *ACS Energy Lett.* **2022**, *7*, 3270.
[46] K. N. Wood, G. Teeter, *ACS Appl. Energy Mater.* **2018**, *1*, 4493.
[47] M. Yang, J. Zhu, S. Bi, R. Wang, Z. Niu, *Adv. Mater.* **2022**, *34*, 2201744.
[48] D. Dong, T. Wang, Y. Sun, J. Fan, Y.-C. Lu, *Nat. Sustain.* **2023**, *6*, 1474.
[49] J. Shi, T. Sun, J. Bao, S. Zheng, H. Du, L. Li, X. Yuan, T. Ma, Z. Tao, *Adv. Funct. Mater.* **2021**, *31*, 2102035.